Selective Mercury Adsorption and Enrichment Enabled by Phenylic Carboxyl Functionalized Poly(pyrrole methane)s Chelating Polymers

Zhenyu Wang [a], Yunpeng Liu [a], Wenlong Zhang [a, c], Yubing Wang [a], Hao Xu [a], Liu Yang [a],

Jiangtao Feng [a,e*], Bo Hou [b*], Mingtao Li [d], Wei Yan [a]

[a] Department of Environmental Engineering, Xi'an Key Laboratory of Solid Waste Recycling and Resource Recovery, School of Energy and Power Engineering, Xi'an Jiaotong University, Xi'an, 710049, China.

[b] School of Physics and Astronomy, Cardiff University, The Parade, Cardiff, CF24 3AA, UK

[c] School of Eco-Environment, Hebei University, Baoding 071002, China (present address)

[d] International Research Center for Renewable Energy (IRCRE), State Key Laboratory of Multiphase Flow in Power Engineering (MFPE), Xi'an Jiaotong University, Xi'an, Shaanxi 710049, China

[e] Jiangsu Engineering Laboratory of New Materials for Sewage Treatment and Recycling, Soochow University, Suzhou, Jiangsu 215123, China

Abstract: Mercury decontamination from water requires highly effective and efficient methods for maintaining public health and environmental protection. Herein, based on the

*Corresponding authors:

Jiangtao Feng: fjtes@xjtu.edu.cn; Bo Hou: HouB6@cardiff.ac.uk

17 coordination theory between functional groups and metal ions, we proposed phenylic carboxyl

18 group-based poly(pyrrole methane)s (PPDCBAs) as highly efficient mercury removal

19 materials for environmental remediation applications. It was found that PPDCBAs can

20 efficiently adsorb and remove mercury(II) from aqueous solutions by functionalizing the

21 molecular structure with phenylic carboxyl groups. Among the as-prepared PPDCBAs,

22 poly[pyrrole-2, 5-diyl (4-carboxybenzylidane)] (PPD4CBA) with the carboxyl group at the

23 *para* position can not only adsorb mercury over 1400 $mg \cdot g^{-1}$ but also achieve a 92.5%

24 mercury(II) uptake within 100 minutes by a very low dosage of 0.1 $g \cdot L^{-1}$. In addition,

25 PPDCBAs exhibited excellent adsorption selectivity for mercury(II) compared with copper(II),

26 cadmium(II), zinc(II) and lead(II). Furthermore, as determined by Fourier transform infrared

27 (FT-IR) spectra, X-ray photoelectron spectroscopy (XPS) and the density functional theory

28 (DFT) calculation, the mercury removal was found to be mainly dependent on the high density

29 of chelating sites, the phenylic carboxyl moieties, which helped us to realize an ultra-trace

30 amount mercury removal (from 10.8 $\mu g \cdot L^{-1}$ to 0.6-0.8 $\mu g \cdot L^{-1}$) for meeting drinking water

31 standard requirements (1.0 $\mu g \cdot L^{-1}$).

32 **Keywords:** poly(pyrrole methane)s, adsorption, mercury, carboxyl groups, density functional

33 theory (DFT)

34 **1. Introduction**

35   Mercury(II) pollution, which can cause severe damage to the brain, kidneys and nervous

36 system (Chen et al., 2021; Dai et al., 2019), has long been a threat to the ecosystem and further

37　public health by invading the human body through the food chain. Mercury is mainly generated

38　from coal combustion, papermaking, oil refining and electroplating, metallurgy, and battery

39　manufacturing (Dong et al., 2013; Velempini and Pillay, 2019; Wang et al., 2016) and exists

40　in various chemical forms such as elemental mercury (Hg^0), inorganic mercury (Hg^{2+}) and

41　methyl mercury (CH_3Hg^+) (Ballav et al., 2018; Holmes et al., 2009; Luo et al., 2015). In order

42　to reduce the harm of mercury(II) to the environment and public health, the World Health

43　Organization (WTO) sets the upper limit of mercury content in wastewater and drinking water

44　as 5 $\mu g \cdot L^{-1}$ and 1 $\mu g \cdot L^{-1}$, respectively (Alguacil and López, 2020; Yan et al., 2021). In addition,

45　according to the Minamata Convention in 2017, monitoring and controlling mercury pollution

46　is imminent (Fu, Y. et al., 2019; Worthington et al., 2017). So it is imperative to develop

47　effective technologies to remove the existing mercury pollution from water until the emissions

48　can be significantly reduced.

49　　Many technologies have been developed for mercury(II) removal from aqueous media, such

50　as chemical precipitation (Brown; et al., 1979; Skyllberg and Drott, 2010), coagulation

51　(Bachand et al., 2019; Henneberry et al., 2011), ion exchange (Alguacil and Escudero, 2020;

52　Anirudhan et al., 2008), membrane separation (Chakrabarty et al., 2010; Mungray and Murthy,

53　2012) and adsorption (Ahmad et al., 2020; Nasimi et al., 2020). In comparison with other

54　methods, adsorption is highly efficient, cost-effective, and environmentally friendly (Ballav et

55　al., 2018). Various adsorbent materials, such as mesoporous silica (Fu, Y. et al., 2019; Gupta

56　et al., 2019), chitosan (Ge and Du, 2020), cellulose (Bisla et al., 2020; Kenawy et al., 2018),

57　carbon materials (Caicedo Salcedo et al., 2021), etc., have been applied to adsorb and remove

58   mercury(II) from wastewater. However, such prevalent adsorbents generally have low

59   adsorption capacity, poor selectivity and weak affinity for mercury(II). For example, the

60   specific surface area of activated carbon made from Mango seeds is 2-33 $m^2 \cdot g^{-1}$, and the

61   adsorption capacity of mercury(II) is only 56.1-85.6 $mg \cdot g^{-1}$ (Caicedo Salcedo et al., 2021). A

62   chemically guanyl-modified cellulose material has very poor adsorption selectivity for

63   mercury(II) (only 48 $mg \cdot g^{-1}$) (Kenawy et al., 2018). Therefore, the development of novel high-

64   efficiency adsorbents will be an important task.

65   Previous literature has shown that the introduction of suitable functional groups can

66   effectively improve the performance of adsorbents (Aguila et al., 2017; Duan et al., 2018; Fu,

67   L. et al., 2019; Li et al., 2019; Li et al., 2014; Zhao et al., 2019). The specific functional groups

68   can not only increase the uptake capacity but also improve the selectivity due to the different

69   affinity between functional groups and heavy metal ions. The sulfhydryl group (-SH) is highly

70   efficient as an adsorption site for mercury, which has been widely reported (Ballav et al., 2018;

71   Leus et al., 2017; Zhang et al., 2012; Zhao et al., 2019). However, the sulfhydryl group is less

72   stable, prone to be oxidized and forming disulfide bonds at higher pH conditions (Choi et al.,

73   2020; Monahan et al., 1995). The carboxylate group (-COO$^-$) is more stable, and can generally

74   coordinate with metal ions in three ways (Lawrance, 2013): only one oxygen is complexed

75   with one metal, each oxygen is combined with one metal separately, or two oxygen are

76   coordinated with one metal to form a more stable chelate. Therefore, we expect to obtain a

77   novel adsorbent that is easily regulated by carboxyl groups to remove mercury(II) from water

78   efficiently.

79   Conductive polymers, including polyaniline (PANI) (Lyu et al., 2019), polythiophene (PTh)

80   (Chen et al., 2019) and polypyrrole (PPy) (Xu et al., 2019), have been used as a new type of

81   adsorbent for efficient removal of heavy metal ions from water because of their good

82   doping/dedoping performance and electrostatic interaction with heavy metal ions (Ji et al.,

83   2021). Poly (pyrrole methane)s, a derivative of polypyrrole, is synthesized via the electrophilic

84   substitution of α-H of pyrrole by protonated aldehydes under acid catalysis, which offers a

85   feasible strategy to create a variety of active sites with good uptake capacities just by adding

86   different aldehydes with functional groups. Furthermore, because of three different substitution

87   sites on the benzene ring, poly(pyrrole methane)s synthesized from aromatic aldehyde can form

88   three steric hindrance structures, which may affect the capture of mercury. Therefore,

89   poly(pyrrole methane)s functionalized with phenylic carboxyl groups at different substitution

90   sites could have distinct mercury capturing abilities. Systematic studies will be needed to

91   determine the efficiency among these promising mercury(II) adsorbents.

92   In this study, poly[pyrrole-2, 5-diyl(benzylidane)] (PPDBA), poly[pyrrole-2, 5-diyl(2-

93   carboxybenzylidane)] (PPD2CBA), poly[pyrrole-2, 5-diyl(3-carboxybenzylidane)]

94   (PPD3CBA) and poly[pyrrole-2, 5-diyl(4-carboxybenzylidane)] (PPD4CBA) were designed

95   and synthesized by one-step chemical polymerization. The as-prepared poly(pyrrole methane)s

96   with carboxyl group in different substitution sites of benzene ring feature the highly accessible

97   mercury(II) binding sites thereby affording strong adsorption selectivity for mercury(II) in the

98   presence of other cations and the efficient mercury(II) capture capacity. The effects of typical

99   anions and cations (e.g., Ca^{2+}, Na^+, K^+, Mg^{2+}, Cl^-, SO_4^{2-}, CO_3^{2-}, NO_3^-) on the Hg(II) removal

100 were also evaluated. Moreover, its practical application value is evaluated in real water

101 matrices. Additionally, the mechanisms for Hg(II) removal are elucidated by the

102 characterization (such as FT-IR, XPS) and density functional theory (DFT) calculations. This

103 work reveals an effective strategy to tune the adsorption performance of poly(pyrrole

104 methane)s as a potential efficient adsorbent for mercury removal.

105 **2. Materials and Methods**

106 *2.1. Materials*

107   Pyrrole (98%), benzaldehyde, 2-carboxybenzaldehyde, 3-carboxybenzaldehyde, 4-

108 carboxybenzaldehyde, hydrochloric acid (HCl), sodium hydroxide (NaOH), nitric acid

109 (HNO$_3$), N,N-Dimethylformamide (DMF), Hg(NO$_3$)$_2$·H$_2$O, Cd(NO$_3$)$_2$·H$_2$O, Cu(NO$_3$)$_2$·H$_2$O,

110 Zn(NO$_3$)$_2$·H$_2$O, Pb(NO$_3$)$_2$·H$_2$O, KNO$_3$, Ca(NO$_3$)$_2$, Mg(NO$_3$)$_2$, NaCl, Na$_2$SO$_4$ were purchased

111 from Sinopharm Chemical Reagent Co., Ltd. All reagents were of analytical grade and used

112 without further purification unless otherwise noted. And the deionized water used in this work

113 was produced by EPED-40TF Superpure Water System (EPED, Nanjing, China).

114 *2.2. Preparation of Poly(pyrrole methane)s.*

115   The poly(pyrrole methane)s were synthesized by one-step chemical polymerization. First,

116 0.02 mol of benzaldehyde was dissolved in 100 mL DMF and poured into a 500 mL three-

117 necked flask. After adding 28.6 mL of hydrochloric acid, 100 mL of DMF containing 0.02 mol

118 of pyrrole was slowly added to the above solution, stirring at 350 rpm. Afterwards, the mixture

119 liquid was kept stirring at 60°C for 6 hours, and then the solution was stirred at room

120   temperature for another 18 hours. Next, the mixture was poured into 800 mL of deionized water

121   with magnetic stirring for 10 minutes to precipitate the product, and then allowed to stand for

122   2 hours. The solid was filtered and washed with deionized water until the filtrate was neutral.

123   The solid obtained was dried at 60°C for 12 h, then ground into powder and sieved with a 100

124   mesh sieve, which is named "PPDBA". The above benzaldehyde was replaced by 2-

125   carboxybenzaldehyde, 3-carboxybenzaldehyde and 4-carboxybenzaldehyde to obtain

126   PPD2CBA, PPD3CBA and PPD4CBAa, respectively.

127   *2.3. Characterizations*

128   Fourier transform infrared (FT-IR) spectra were scanned in the region of 500-4000 cm^{-1} using

129   KBr pellets on a Bruker TENSOR 37 FT-IR spectrophotometer. The pH values of the solution

130   were detected by a pH meter (FE28-Standard, Mettler Toledo). The morphology was examined

131   by scanning electron microscope (SEM, Zeiss Gemini SEM 500). The X-ray photoelectron

132   spectroscopy (XPS) spectra were performed on Kratos Axis Ultra DLD with an Al

133   monochromatic X-ray source (1486.71 eV), and all the binding energies (BEs) were revised

134   according to the C 1s hydrocarbon peak at 284.8 eV. The ^{1}H NMR spectra (Bruker III HD 400

135   M) were used to confirm the chemical structures of the as-prepared samples. The Barrett-

136   Emmett-Teller specific surface area (S_{BET}), total pore volume (V), and average pore radius (R)

137   were performed by a physical adsorption device (SSA-4200, Beijing Builder Co. Ltd, China).

138   Zeta potentials were determined on a Malvern Zetasizer Nano ZS90 at the pH value range of

139   2-12.

2.4. Batch Adsorption Studies

All solutions containing cations are prepared from corresponding nitrates in the adsorption experiments, and the solutions containing anions are corresponding sodium. The simulated solution used in the experiments was prepared by diluting the 5 mmol·L^{-1} Hg(NO$_3$)$_2$ stock solution with deionized water, and the initial pH value was adjusted by 0.1 mol·L^{-1} NaOH or HNO$_3$ solution. The 50 mL centrifuge tubes containing 2 mg adsorbent and 20 mL of 0.5 mmol·L^{-1} heavy metal ion solution were ultrasonically treated for 2 minutes to achieve uniform dispersion of the adsorbent in the liquid, and then transferred in a constant temperature shaker to adsorb at 220 rpm for 24 hours at 298 K. After the adsorption reaction, the solution filtered by a 0.45 μm-filter was analyzed by the inductively coupled plasma optical emission spectrometer (ICP-OES, ICPE-9000, Japan) to determine the concentration of heavy metal ions. The adsorption efficiency (η) and equilibrium adsorption capacity (Q_e) were calculated from the Eq. (1) and (2).(Liu et al., 2019)

$$\eta = \frac{C_0 - C_e}{C_0} \times 100\% \tag{1}$$

$$Q_e = \left(\frac{C_0 - C_e}{m} \right) V \tag{2}$$

where C_0 and C_e (mg·L^{-1}) are the initial and equilibrium concentrations of heavy metal ions in solution, respectively, m (g) is the adsorbent mass, and V (L) is the volume of solution.

For the kinetics study, 40 mg PPDCBAs were added to 10 mL of deionized water and the mixture was treated with ultrasound for 2 minutes, then poured into the 400 mL of 0.5 mmol·L^{-1} Hg(II) solution at pH 5-6. The reaction system was stirred with magnetic stirring at a speed

158   of 220 rpm and kept at 298 K with an oil bath. At time zero and preselected time intervals (0-

159   420 min), 2 mL samples were taken out and filtered quickly with polyethersulfone membrane

160   for Hg(II) concentration analysis.

161   To investigate the pH effect on Hg(II) removal by the as-prepared samples, the solution's

162   initial pH values were adjusted from 2 to 6 with 0.1 mol·L^{-1} HNO$_3$ or NaOH solution. Different

163   dosages are designed in the range of 0.05-1.0 g L^{-1} at an initial concentration of 100 mg·L^{-1}

164   (pH = 5.5, T = 25 °C) to study the effect of adsorbent dosage. In addition, adsorption isotherm

165   studies were carried out by changing the initial concentration of Hg(II) from 0.05 to 1 mmol·L^{-1}

166   at four different temperatures (288 K, 298 K, 308 K, 318 K).

167   The effect of background ions (Na$^+$, Ca^{2+}, Mg^{2+}, K$^+$, SO$_4^{2-}$, Cl$^-$) was investigated in a binary

168   adsorption mode, and the concentration of background ions was 10 mmol·L^{-1}. Furthermore, in

169   order to study the selective adsorption performance of the adsorbent, mixed solutions were

170   explored. The competitive heavy metal ions included Pb(II), Cd(II), Cu(II) and Zn(II), with the

171   same concentration of 0.5 mmol·L^{-1} of Hg(II).

172   In addition, batch adsorption-desorption experiments were carried out to investigate the

173   regeneration and reusability of PPDCBAs. Typically, 15 mg of PPDCBAs was mixed into 150

174   mL of Hg(II) solution (0.5 mmol·L^{-1}, pH=5.5). Then the desorption and regeneration of

175   exhausted PPDCBAs were accomplished with a 150 mL solution containing 0.1 mol·L^{-1} HCl

176   and 1 wt% thiourea and vibrating for 3 h at 298 K (Duan et al., 2018; Fu et al., 2022). Then,

177   the adsorbent was filtered and washed with deionized water until the filtrate was neutral for the

178   next adsorption-desorption cycle.

179   *2.5. Density functional theory calculation details*

180   The density functional theory (DFT) calculation was employed for further confirmation of

181   the adsorption mechanism. The simulation was carried out by the Gaussian 09W software

182   package using the B3LYP-D3 function, where D3 denotes the third-generation dispersion

183   correction by Grimme. The solvation effect (H_2O) was evaluated with solvation model based

184   on density (SMD) (Marenich et al., 2009). For structural optimization and frequency

185   calculation, the 6-31+G(d) basis set was applied for the description of C, H, N, and O atoms,

186   whereas the LANL2DZ basis set was used for Hg (Fu, T. et al., 2019). And static calculation

187   was conducted using LANL2DZ basis set for Hg and 6-311++G(d, p) basis set for other atoms

188   (Fu, T. et al., 2019; Zhao et al., 2019).

189   The adsorption energy (ΔE_{ad}) was calculated to evaluate the affinity between adsorbent

190   materials and heavy metals by Eq. (3) (Oyetade et al., 2017).

$$\Delta E_{ad} = E_{complex} - (E_{metal} + E_{material}) \tag{3}$$

191   where $E_{complex}$, E_{metal} and $E_{material}$ are the energy (kJ·mol^{-1}) of the metal ion-adsorbent complex,

192   metal ion and adsorbent material, respectively.

193   **3.   Results and Discussion**

194   *3.1. Characterization of the poly(pyrrole methane)s*

195   Fig. 1 exhibits the FT-IR spectra of the four poly(pyrrole methane)s. The peaks at around

196   3435 cm^{-1} are the N–H stretch of the pyrrole ring (Ji et al., 2021; Liu et al., 2019), the weak

197   peaks at about 3100-3000 and 3000-2900 cm^{-1} are related to the C–H stretch of a benzene ring

198   and backbone (Liu et al., 2019), respectively. The C=C stretching of the benzene ring in

199   PPDBA, PPD2CBA, PPD3CBA and PPD4CBA appear at 1593, 1633, 1604 and 1608 cm^{-1},

200   respectively. The peaks at 1565 and 1407 cm^{-1} in PPDBA, 1576 and 1393 cm^{-1} in PPD2CBA,

201   1558 and 1387 cm^{-1} in PPD3CBA, 1540 and 1389 cm^{-1} in PPD4CBA are consistent with C=C

202   stretching and C–N stretching of the pyrrole ring, respectively (Anirudhan et al., 2008; Xu et

203   al., 2019). Compared with the PPDBA, the new adsorption bands at 3266, 1755 and 1287 cm^{-1}

204   in PPD2CBA, 3238, 1698 and 1266 cm^{-1} in PPD3CBA, 3258, 1699 and 1269 cm^{-1} in

205   PPD4CBA are attributed to –OH stretching, C=O stretching and C–O stretching of the carboxyl

206   group on the benzene ring, respectively (Ballav et al., 2018; Saleh, 2015; Xu et al., 2019).

207   However, it should be noted that the absorption peaks of –OH and C=O on the carboxyl group

208   of PPD2CBA are quite different from those on the other two samples, which is mainly caused

209   by the number of carboxyl groups. Since PPD3CBA and PPD4CBA contain more carboxyl

210   groups, hydrogen bonds are easily formed between the carboxyl groups, which will extend the

211   stretching peak of –OH to about 2500 cm^{-1}, and shift the stretching of C=O from 1755 to 1700

212   cm^{-1} (Bakker et al., 2003; I.D.Reva and S.G.Stepanian, 1995; Toru Yahagi et al., 2001). The

213   results of FT-IR indicated that the four poly(pyrrole methane)s were successfully synthesized
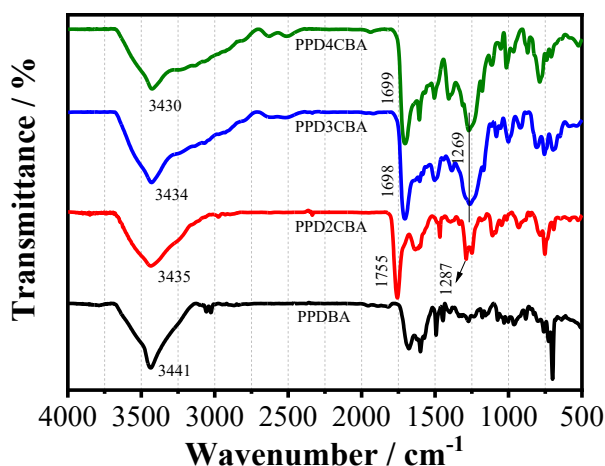
214   in this work.

Fig. 1. FT-IR spectra of as-prepared PPDCBAs derivatives.

Fig. S1 shows the ^{1}H NMR spectra of the samples. PPDBA: ^{1}H NMR (500 MHz, DMSO-d$_6$, δ): 10.87-10.12 (broad, 1H, NH), 7.84-6.59 (m, 7H, Pyr-H and Ar-H), 5.34 (s, 1H, (Pyr)$_2$-CH-Ar). PPD2CBA: ^{1}H NMR (500 MHz, DMSO-d$_6$, δ): 12.38 (s, 1H, COOH), 11.25-10.87 (broad, 1H, NH), 7.93-6.62 (m, 6H, Pyr-H and Ar-H), 5.56 (s, 1H, (Pyr)$_2$-CH-Ar). PPD3CBA: ^{1}H NMR (500 MHz, DMSO-d$_6$, δ): 12.95 (s, 1H, COOH), 10.86-10.12 (broad, 1H, NH), 8.45-6.89 (m, 6H, Pyr-H and Ar-H), 5.38 (s, 1H, (Pyr)$_2$-CH-Ar). PPD4CBA: ^{1}H NMR (500 MHz, DMSO-d$_6$, δ): 12.94 (s, 1H, COOH), 10.89-10.25 (broad, 1H, NH), 8.40-6.89 (m, 6H, Pyr-H and Ar-H), 5.38 (s, 1H, (Pyr)$_2$-CH-Ar) (Li et al., 2015). It is noted that the chemical shift of ^{1}H on the carboxyl group in PPD2CBA is lower than that in PPD3CBA and PPD4CBA, which is because more carboxyl groups in PPD3CBA and PPD4CBA strengthened the hydrogen bonds between the sample molecules and reduced the shielding effect of active hydrogen, increasing the chemical shift.

As depicted in Fig. S2, exposure of PPDCBAs to water at different pH (pH = 2-6) for 2 days caused no obvious changes in molecular structure, which indicated that PPDCBAs had

231   excellent stability under the current pH range. In addition, TG curves showed that poly(pyrrole

232   methane)s still had good thermal stability when the temperature reached 200 °C (Fig. S3).

233   The elemental analysis result show that PPD4CBA and PPD3CBA have higher oxygen

234   content (Table 1), which means that they may contain more carboxyl groups, which is

235   consistent with the results of FT-IR and NMR. The oxygen in PPDBA may come from the

236   adsorbed water. The difference in oxygen content may be due to the influence of the spatial

237   position of carboxyl and aldehyde groups on the electrophilic substitution reaction in the

238   polymerization process.

239   **Table 1.** Content of C, N, H and O elements in the four prepared adsorbents

	Adsorbents	C%	N%	H%	O%
Test Value	PPDBA	81.25	8.47	5.20	1.9
	PPD2CBA	70.53	6.97	4.10	13.6
	PPD3CBA	67.18	6.43	4.42	18.4
	PPD4CBA	66.47	6.58	4.46	18.9
Theoretical Value	PPDBA	85.16	9.03	5.81	---
	PPDCBAs	72.36	7.04	4.52	16.08

240   The morphologies of the poly(pyrrole methane)s are characterized by SEM. As shown in Fig.

241   S4, all of them show irregular, short rod-shaped or spherical skeletons like aggregate. Pore

242   structure and specific surface area of the as-prepared poly(pyrrole methane) are shown in Table

243   S1 and Fig. S5. Obviously, PPD4CBA has a larger specific surface area (S_{BET}, 106.92 $m^2 \cdot g^{-1}$)

244   and pore volume (V, 0.76 $cm^3 \cdot g^{-1}$) than the other three samples.

245   *3.2. Investigation of adsorption properties*

246   *3.2.1.   Effect of initial pH*

247   The impact of the initial pH of the solution on the adsorption is shown in Fig. 2a. The result

248   indicates that the adsorption capacity of Hg(II) onto the poly(pyrrole methane)s is highly pH-

249   dependent. The capture capacity increases with pH from 2 to 4 and reaches a plateau at pH

250   from 4 to 7. Generally, for mercury ions, Hg^{2+} and $Hg(OH)^+$ are the dominant species in the

251   solution at pH of 2-3 without Cl^- (Fig. 2b). Meanwhile, PPDCBAs are positively charged as

252   their pH is below the pH_{zpc} (Fig. 2c). So, the low adsorption capacity for mercury at this pH

253   may be attributed to electrostatic repulsion between positively charged mercury and adsorbent

254   surface as well as the competition from H^+ in the solution. With the increase of pH, mercury(II)

255   is gradually converted to neutral $Hg(OH)_2(aq)$. The electrostatic repulsion with the adsorbent

256   is negligible for the neutral $Hg(OH)_2(aq)$ is the dominant species at pH range 4-7.(Dong et al.,

257   2013) Meanwhile, the complexation of $Hg(OH)_2(aq)$ with carboxylic groups in PPDCBAs is

258   likely more favored because carboxylic groups became more deprotonated ($=COO^-$) at this pH

259   range (Dong et al., 2013). Furthermore, $Hg(OH)_2$ has better mobility due to the smaller

260   "effective molecular size" than Hg^{2+} and $Hg(OH)^+$ (Zhang et al., 2012).

261   *3.2.2.   Effect of dosage*

262   The optimal adsorbent dosage is a critical parameter for the purification of wastewater by

263   adsorption. Fig. 2d and Fig. S6 show the removal rate and adsorption capacity of Hg(II) with

264   respect to the adsorbent dosage, respectively. The removal rate increases rapidly as a function

265   of dosages loading, which can be attributed to the increase of available adsorption sites.

266   Eventually, the removal rate of mercury gradually reaches 100% for PPDCBAs. However, the

267   removal rate of Hg(II) remains basically invariant for PPDBA as the dosage increases, owing

268   to fewer adsorption sites of PPDBA. Furthermore, even at a low dosage (0.1 g·L⁻¹), the removal

269   rate of Hg(II) by PPD3CBA and PPD4CBA can still reach above 90%, and PPDCBAs maintain

270   high adsorption capacity. Therefore, the dosage of 0.1 g·L⁻¹ was chosen as a standard in the
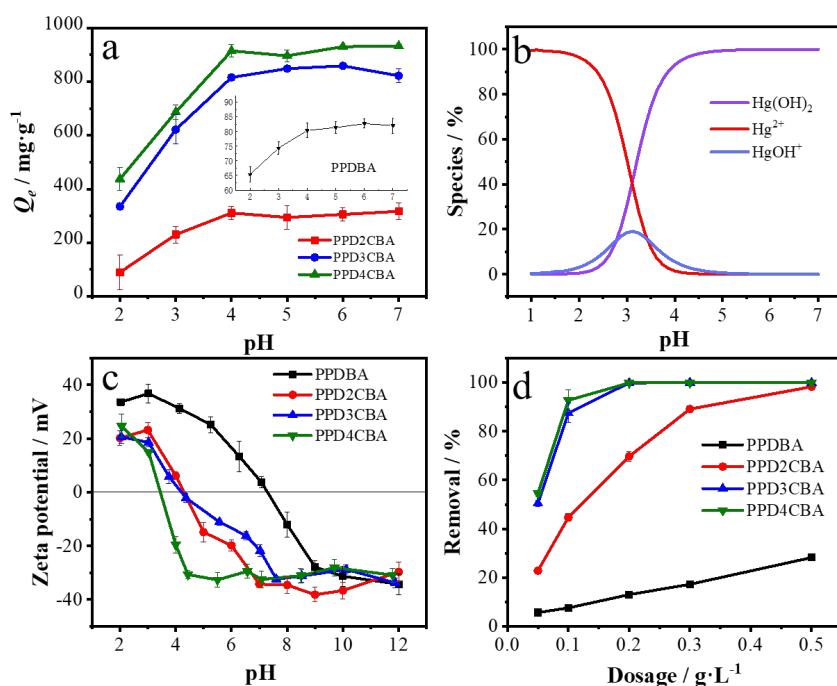
271   following experiments.

272

273   **Fig. 2.** Effect of initial solution pH on the Hg(II) adsorption ($C_0 = 100$ mg·L⁻¹, dosage = 0.1·g·L⁻

274   ¹, T = 298 K, pH = 2-7) (a), Morphological distribution of Hg(II) at different pH in the absence

275   of chloride (b), Zeta potentials of the adsorbents (c), Effect of dosage on the removal of Hg(II)

276   ($C_0 = 100$ mg·L⁻¹, dosage = 0.05-0.5·g·L⁻¹, T = 298 K, pH=5.5) (d).

277   *3.2.3.   Adsorption kinetics*

278   The influence of the contact time on Hg(II) adsorption by PPDCBAs is shown in Fig. 3a.

279   Hg(II) adsorption onto PPDCBAs increased rapidly in the initial 30 min and reached a plateau

280   afterwards. And the initial adsorption rate of three PPDCBAs followed the order of PPD4CBA

281   > PPD3CBA > PPD2CBA. The adsorption equilibrium of the PPDCBAs reached within 100

282   min.

283   Pseudo-first-order (PFO) model and pseudo-second-order (PSO) model are always employed

284   to evaluate the kinetic data. The differential form of the PFO model and PSO model are

285   described in Eq. (4) and (5) (Wang and Guo, 2020), respectively.

$$\frac{dQ_t}{dt} = k_1(Q_e - Q_t) \tag{4}$$

$$\frac{dQ_t}{dt} = k_1(Q_e - Q_t)^2 \tag{5}$$

286   where Q_t (mg·g^{-1}) and Q_e (mg·g^{-1}) are the adsorption capacity at time t (min) and equilibrium

287   respectively, k_1 (min^{-1}) and k_2 (g·mg^{-1}·min^{-1}) are the rate constants for the pseudo-first-order and

288   pseudo-second-order, respectively.

289   Integrating Eq. (4) and (5) for the conditions of $Q_0 = 0$ yields Eq. (6) and (7), respectively.

$$Q_t = Q_e(1 - e^{-k_1 t}) \tag{6}$$

$$Q_t = \frac{k_2 Q_e^2 t}{1 + k_2 Q_e t} \tag{7}$$

290   PFO and PSO models are applicable to three different hypotheses and conditions,

291   respectively. Firstly, the high C_0 value is applicable to the PFO model, while the low C_0 value

292   is applicable to PSO model; Secondly, PFO model can better describe the initial stage of the

293 adsorption process, while PSO model is more suitable for the adsorption process at the final

294 stage; Finally, the adsorption materials with few adsorption sites can be better described by

295 PFO model. Therefore, the adsorption is not only determined by the active sites, and in some

296 cases, the PFO model can be dominated by external/internal diffusion. However, the adsorption

297 materials with abundant active sites can be well modelled by the PSO model, which means the

298 adsorption kinetics is dominated by the adsorption onto the active site (Wang and Guo, 2020).

299   In addition, the Elovich model has been extensively applied to chemisorption data, which

300 was described by Eq. (8) (Elovich and Larinov, 1962; Tran et al., 2017).

$$\frac{dQ_t}{dt} = \alpha e^{-\beta Q_t} \tag{8}$$

301 where α (mg·g^{-1}·min^{-1}) reflects the initial adsorption rate because $dQ_t/dt \to \alpha$ when $Q_t \to 0$, and

302 β (mg·g^{-1}) is the desorption constant during any one experiment.

303   By applying the boundary conditions of $Q_t = 0$ at $t = 0$, the integrated form of Eq. (8) will

304 become Eq. (9)

$$Q_t = \frac{1}{\beta} \ln(1 + \alpha\beta t) \tag{9}$$

305   Table S2 depicts the kinetic parameters for the three models. It can be observed that the PSO

306 ($R^2 = 0.9518$-0.9703) could better describe the adsorption kinetics of PPDCBAs for Hg(II)

307 compared with PFO ($R^2 = 0.8920$-0.9112), suggesting that the adsorption kinetics is dominated

308 by the adsorption onto the active site. The Elovich model with the larger correlation coefficients

309 ($R^2 = 0.9829$-0.9987) further indicated that the adsorption of Hg(II) onto PPDCBAs involved

310 a chemical adsorption process. Moreover, the relatively bigger rate constant α indicated that

311 PPD4CBA had a higher initial adsorption rate (Lin et al., 2018).

312   In addition, the diffusion mechanism was further evaluated by analyzing the role of intra-

313   particle diffusion in the adsorption process. The linearized transformation of the intra-particle

314   diffusion model is presented as Eq. (10) (Tran et al., 2017).

$$Q_t = k_i t^{\frac{1}{2}} + C_i \tag{10}$$

315   where k_i (mg·g^{-1}·min$^{-1/2}$) is the intra-particle diffusion rate constant and C_i (mg·g^{-1}) is a constant

316   associated with the thickness of the boundary layer, where a higher value of C_i corresponds to

317   a greater effect on the limiting boundary layer.

318   Linear plots of the intra-particle diffusion model for all three adsorbents are depicted in Fig.

319   3b. It can be seen that the adsorption process can be divided into three linear regions with

320   different slopes, which indicates that the adsorption process is affected by multiple diffusion

321   steps. The initial sharp linear region could be attributed to the surface adsorption of Hg(II),

322   which was controlled by boundary layer diffusion. In the second stage, the adsorption rate

323   slowed down gradually, indicating that intra-particle diffusion was the rate-limiting mechanism

324   during this stage. In the last stage, due to the decrease in the Hg(II) concentration in solution,

325   the diffusion rate in the particles further slowed down, thus reaching the final equilibrium stage.

326   *3.2.4.   Adsorption isotherm*

327   Adsorption isotherms play a vital role in evaluating the adsorption capacities of adsorbents

328   and investigating chemical interactions between adsorbate and adsorbents. Langmuir and

329   Freundlich isotherms are widely used to analyze the adsorption isotherm data, and their non-

330   linear formulas are given by Eq. (11) and (12), respectively (Al-Ghouti and Da'ana, 2020;

331   Zhang, Y. et al., 2021). The basic assumptions of the Langmuir isotherm are: (1) monolayer

332   adsorption; (2) the distribution of adsorption sites is homogeneous; (3) the adsorption energy

333   is constant; and (4) the interaction between adsorbate molecules is negligible. And the

334   Freundlich equation is one of the earliest empirical equations used to describe equilibrium data

335   and adsorption characteristics for a heterogeneous surface (Freundlich, 1907). Unlike the

336   Langmuir isotherm model, Freundlich model is not restricted to the monolayer formation in

337   which its application to the multilayer adsorption is possible (Al-Ghouti and Da'ana, 2020).

$$Q_e = \frac{Q_{max} K_L C_e}{1 + K_L C_e} \tag{11}$$

$$Q_e = K_F C_e^{1/n} \tag{12}$$

338   where C_e (mg·L^{-1}) is the heavy metal ion concentration at adsorption equilibrium; Q_e (mg·g^{-1})

339   and Q_{max} (mg·g^{-1}) are the equilibrium adsorption capacity and the maximum monolayer

340   adsorption capacity, respectively; K_L (L·mg^{-1}) is the Langmuir constant which is related to the

341   affinity of adsorbate and the binding sites; K_F ((mg·g^{-1})/(mg·L^{-1})$^{1/n}$) is the Freundlich constant

342   indicating the relative adsorption capacity of the adsorbents. n is a dimensionless constant

343   related to the intensity of adsorption.

344   In addition, the dimensionless separation factor R_L can estimate the favorability of the

345   adsorption and is expressed by Eq. (13) (Al-Ghouti and Da'ana, 2020; Hall et al., 1966).

$$R_L = \frac{1}{1 + K_L C_0} \tag{13}$$

346   where C_0 (mg·L^{-1}) is the initial concentration of adsorbate. The value of R_L indicates

347   irreversible adsorption when $R_L = 0$, favorable adsorption when $0 < R_L < 1$, linear case when R_L

348   = 1 or unfavorable adsorption when $R_L > 1$.

349   According to Fig. 3c-e and Table S3, Langmuir model fits better than the Freundlich model

350   for all PPDCBAs, suggesting that the adsorption process is monolayer adsorption.(Xu et al.,

351   2019) Meanwhile, according to the calculation based on experimental data, the values of R_L are

352   in the range of 0 to 1, which indicates the adsorption process is favorable under operating

353   conditions (Al-Ghouti and Da'ana, 2020). Moreover, as the temperature increases from 288 K

354   to 328 K, the maximum adsorption capacity (Q_{max}) of Hg(II) onto PPD2CBA, PPD3CBA and

355   PPD4CBA increased from 406.82 to 875.14 mg·g^{-1}, from 862.62 to 1234.66 mg·g^{-1} and from

356   919.75 to 1427.18 mg·g^{-1}, respectively. In conclusion, it is believed that Hg(II) adsorption is

357   achieved by forming monolayers on the limited adsorption sites on the homogeneous surface

358   (Xu et al., 2019). The comparisons of the adsorption performance of various adsorbents for

359   Hg(II) are shown in Fig. S7 and Table S4. The PPDCBAs offer good adsorption properties for

360   Hg(II) with a very low usage dose (0.1 g·L^{-1}) at a wide pH range.
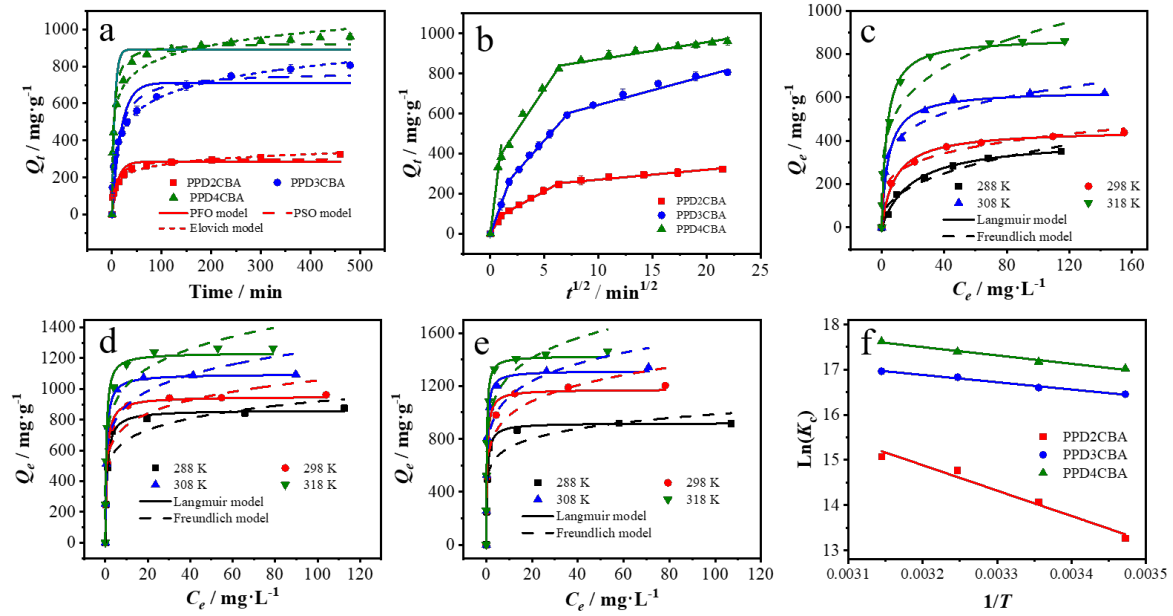
Fig. 3. Adsorption kinetics plots and fitting curves of Hg(II) onto PPDCBAs (a), intra-particle diffusion model for adsorption of Hg(II) onto PPDCBAs (b)(C_0 = 100 mg·L^{-1}, Dosage = 0.1·g·L^{-1}, T = 298 K, pH=5.5), adsorption isotherms for the adsorption of Hg(II) onto PPD2CBA, PPD3CBA and PPD4CBA (c-e) (C_0 = 100 mg·L^{-1}, dosage = 0.1·g·L^{-1}, T = 288-318 K, pH = 5.5), the plots to determine the thermodynamic parameters of Hg(II) adsorption onto PPDCBAs (f).

3.2.5. Thermodynamic parameters

According to Fig. 3c-e and Table S3, the maximum adsorption capacities increase with increasing temperature. Thermodynamic parameters, such as entropy change (ΔS, kJ·mol^{-1}·K^{-1}), enthalpy change (ΔH, kJ·mol^{-1}) and the standard free energy change (ΔG, kJ·mol^{-1}) can be derived based on Eq. (14-16) (Tran et al., 2017; Zhou and Zhou, 2014).

$$\ln K_C = \frac{-\Delta H}{RT} + \frac{\Delta S}{R} \tag{14}$$

$$K_C = \ln(M_W \times 55.5 \times 1000 \times K_L) \tag{15}$$

$$\Delta G = \Delta H - T\Delta S \tag{16}$$

373   where K_C is a dimensionless standard equilibrium constant. 55.5 is the mole concentration of

374   water in mol·L^{-1}, K_L is the Langmuir constant in L·g^{-1}, and M_W (g·mol^{-1}) is the molecular weight

375   of the adsorbate. R (8.314 J·mol^{-1}·K^{-1}) is the universal gas constant, and T is the temperature in

376   K.

377   ΔS and ΔH are calculated from the intercept and slope of the plot of ln K_d versus $1/T$ (Fig.

378   3f). The obtained values of ΔG, ΔH and ΔS under different temperatures are listed in Table

379   S5. The negative ΔG and positive ΔH indicate that the Hg(II) adsorption process is

380   spontaneous and endothermic (Xu et al., 2019). And the positive values of ΔS indicate that the

381   randomness at the solid-liquid interface increases in the adsorption process of Hg(II) (Liu et

382   al., 2019). Moreover, the ΔG values decrease with increased temperature, suggesting increased

383   spontaneity with temperature.

384   *3.2.6.   Effect of the co-existing ions on Hg(II) adsorption*

385   In addition to heavy metals, other ions (e.g., Ca^{2+}, Na^+, K^+, Mg^{2+}, Cl^-, SO_4^{2-}, NO_3^-) widely

386   exist in various water bodies, which may have a negative impact on the adsorption process. In

387   view of this, the effect of selected ions (Na^+, K^+, Ca^{2+}, Mg^{2+}, Cl^-, SO_4^{2-}) on the removal of

388   Hg(II) by PPDCBAs was studied. As shown in Fig. 4a, the co-existing ions such as Na^+, K^+,

389   Ca^{2+}, Mg^{2+}, and SO_4^{2-} do not impact Hg(II) adsorption, which also indicates that NO_3^- has no

390   effect on the adsorption of mercury because the cations are all from the corresponding nitrate.

391   However, Cl^- has an apparent inhibitory effect, which is consistent with the literature reports

392 (Jainae et al., 2015; Zhu et al., 2017). This is because mercury species are complicated by the

393 high chloride ion concentration (10 mmol·L^{-1} NaCl) (Fig. 4b) (Jainae et al., 2015; Lu et al.,

394 2014; Zhu et al., 2017). According to the calculation, under the condition of pH = 5-6, Cl$^-$ and

395 Hg(II) will form multiple complexes, in which HgCl$_2$ is the dominant species, reaching nearly

396 90%, HgCl$_3^-$ accounts for nearly 10%, but Hg(OH)$_2$ and HgClOH are trace amounts. Then

397 different concentrations of NaCl are added to further explore the effect of Cl$^-$ on Hg(II)

398 adsorption. Fig. 4c shows the adsorption capacity of PPD4CBA for Hg(II) and the

399 morphological distribution of Hg at pH=5.5 at different Cl$^-$ concentrations, respectively. As the

400 concentration of Cl$^-$ increases, the adsorption capacity has the same trend with Hg(OH)$_2$ content

401 but the opposite trend with HgCl$_2$ content, indicating that Hg(OH)$_2$ is an important species to

402 be adsorbed but HgCl$_2$ is hardly adsorbed. In addition, when the concentration of Cl$^-$ is 1.0

403 mmol, the amount of Hg(OH)$_2$ only accounts for 2%, but PPD4CBA still has an adsorption

404 capacity of more than 440 mg·g^{-1}, indicating that HgClOH may contribute a part of the

405 adsorption capacity. And as shown in Fig. 4d, the adsorption capacity of PPD4CBA for Hg(II)

406 has a good positive linear relationship with the percentage of Hg(OH)$_2$ plus HgClOH, which

407 further indicates that Hg(OH)$_2$ and HgClOH are active species and have much stronger affinity

408 with the adsorbent than HgCl$_2$. On the one hand, Hg(OH)$_2$ and HgClOH has a smaller "effective

409 molecular size" and higher mobility than HgCl$_2$ (Afaneh et al., 2012; Nightingale, 1959). On

410 the other hand, Hg(OH)$_2$ is more accessible to interact with the active adsorption sites due to

411 the hydrogen bond between hydroxyl and carboxyl (Zhang et al., 2020).

412   Selectivity is an important parameter for adsorbents in practical applications since several

413   co-existing heavy metal ions may also be present in Hg(II)-containing wastewater. Therefore,

414   the possible interference of various co-existing ions (Cu(II), Cd(II), Pb(II), and Zn(II)) on

415   Hg(II) adsorption was investigated. As noted in Fig. 4e, PPDCBAs exhibit high adsorption

416   selectivity for Hg(II), and competition from co-existing ions rarely disturbs the adsorption of

417   Hg(II). The results show that PPDCBAs have a much stronger affinity for Hg(II). In addition,

418   distribution coefficients (K_d, L·g^{-1}) and selectivity coefficient (α) calculations were calculated

419   to investigate the affinity and selectivity degree of adsorbents. The large K_d values indicate that

420   PPDCBAs can well remove the metal ions. K_d and α could be illustrated as Eq. (17, 18) (Lin

421   et al., 2019; Wang et al., 2014).

$$K_d = \frac{Q_e}{C_e} \tag{17}$$

$$\alpha = \frac{K_d(Hg)}{K_d(M_i)} \tag{18}$$

422   where $K_d(Hg)$ and $K_d(M_i)$ represent the distribution coefficients of Hg(II) and co-existing ions,

423   respectively.

424   As noted in Table 2, the K_d value of Hg(II) exceeds that of interfering ions, suggesting that

425   PPDCBAs have an adsorption affinity for Hg(II) that surpasses interfering ions by a wide

426   margin. In addition, the adsorption capacity of PPDCBAs for Cu(II) and Pb(II) is slightly

427   higher than that of Cd(II) and Zn(II), which is related to the existence form of ions under

428   experimental conditions. Cu(II) and Pb(II) form part of hydroxide, while Cd(II) and Zn(II)

429   basically exist in the form of M^{2+} at pH = 5-6 (Fig. S8). This illustrates that PPDCBAs have a

430   stronger affinity for the complex of heavy metals and hydroxide than other M^{2+}, which further

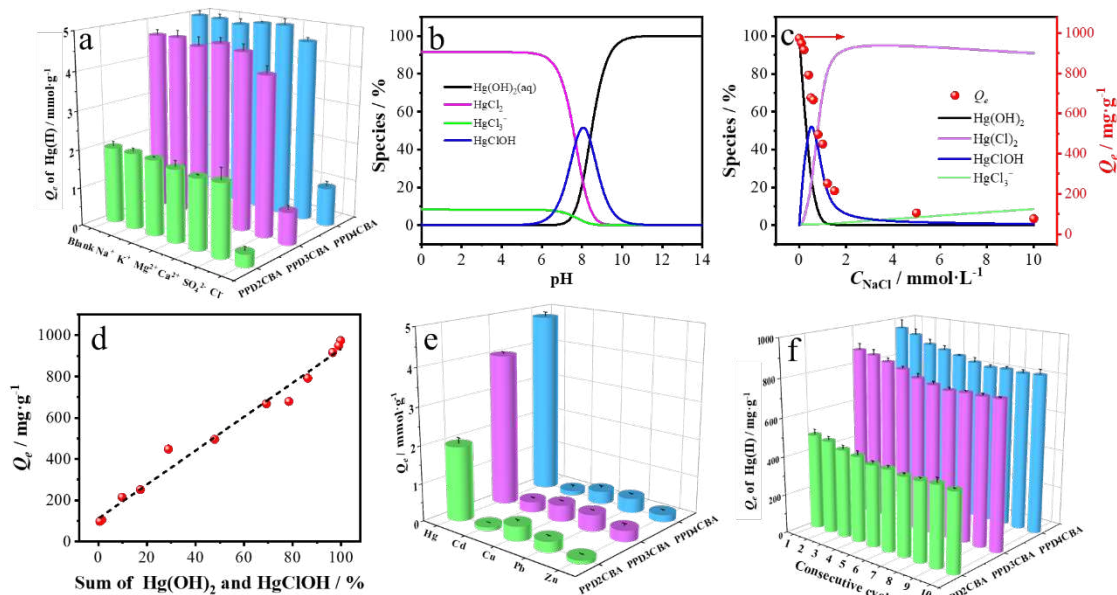431   proves the effect of initial pH on mercury adsorption.

432

Fig. 4. Effect of background ions on the removal of Hg(II) by PPDCBAs ($C_0 = 0.5$ mmol·L^{-1},

dosage = 0.1·g·L^{-1}, T = 298 K, pH = 5.5, the concentration of background ions is 10 mmol·L^{-1}) (a), Morphological distribution of Hg(II) at different pH at NaCl concentration of 10 mmol·L^{-1} (b), Adsorption capacity of PPD4CBA for Hg(II) and the morphological distribution of Hg at pH=5.5 at different Cl$^-$ concentrations (c), The linear relationship between the adsorption capacity of PPD4CBA and the ratio sum of Hg(OH)$_2$ and HgOHCl (d), Effect of co-existing heavy metal ions on the removal of Hg(II) by PPDCBAs ($C_M = 0.5$ mmol·L^{-1}, dosage = 0.1·g·L^{-1}, T = 298 K, pH = 5.5) (e), Adsorption-desorption cycles of Hg(II) onto PPDCBAs (f).

Table 2. The distribution coefficient and selectivity coefficient of heavy metal adsorbed by PPDCBAs

Metal ions	PPD2CBA	PPD3CBA	PPD4CBA

	K_d (L·g⁻¹)	α	K_d (L·g⁻¹)	α	K_d (L·g⁻¹)	α
Hg	6.12	—	34.12	—	127.02	—
Pb	0.64	9.53	1.05	32.38	0.93	137.18
Cu	0.94	6.50	1.06	32.07	0.81	155.88
Zn	0.19	32.46	0.59	58.01	0.37	339.53
Cd	0.19	31.57	0.57	60.21	0.25	511.72

3.3. Evaluation of real application

443

444   Compared with other heavy metals, the emission limit of mercury in drinking water is more

445   stringent. Less than 1 $\mu g \cdot L^{-1}$ is restricted by WHO. The adsorption method is commonly used

446   in the advanced treatment of heavy metal wastewater, and the initial mercury content is usually

447   very low (Fu et al., 2022; Richard and Biester, 2016). It is hoped that the adsorbent can remove

448   the low mercury concentration below the emission limit. As shown in Table 3, the

449   concentration of mercury in the solution can be reduced to less than 1 $\mu g \cdot L^{-1}$ after adsorption,

450   which indicates that PPDCBAs can remove trace Hg(II) effectively, proving their potential

451   value in practical applications.

452   To deeply determine the real application potential of PPDCBAs on Hg(II) removal, the

453   performance of PPDCBAs was further investigated in tap water and Weihe River water

454   matrices. The concentrations of typical anions (e.g., F^-, Cl^-, SO_4^{2-}, NO_3^-, etc.) and COD are

455   shown in Table S6. As the typical Hg(II) concentrations in surface water/groundwater range

456   from 0.001 to 0.87 $mg \cdot L^{-1}$, therefore, the tap water and Weihe river water were spiked with 0.1

457   $mg \cdot L^{-1}$ and 0.3 $mg \cdot L^{-1}$ Hg(II), respectively. As displayed in Table 3, over 95% of Hg(II) was

458   successfully removed by PPDCBAs. Based on the above results, the applicability of PPDCBAs

459   to remove Hg(II) in real water matrices is fully validated.

460   **Table 3** Removal result of trace mercury in different types of water by PPDCBAs.

Water type	pH		The concentration of Hg(II)[a] / $\mu g \cdot L^{-1}$		
			PPD2CBA	PPD3CBA	PPD4CBA
Deionized water	6.74	Before adsorption		10.8	
		After adsorption	0.739	0.827	0.623
		Removal rate / %	93.1	92.3	94.2
Tap water	7.88	Before adsorption		107	
		After adsorption	---	5.18	5.30
		Removal rate / %	---	95.2	95.0
Weihe River water	7.98	Before adsorption		313	
		After adsorption	---	11.4	12.0
		Removal rate / %	---	96.4	96.2

461   [a] The concentration of mercury was detected by inductively coupled plasma mass spectrometer.(ICP-MS, NexION
462   350D)

463   The regeneration performance of the adsorbent is of great significance in evaluating the

464   practical application value. In many reports, mixed solutions of acid and thiourea have been

465   used to achieve effective desorption of mercury (Duan et al., 2018; Fu et al., 2022). On the one

466   hand, thiourea, as a small molecule substance rich in sulfur and nitrogen, has a very strong

467   binding ability with mercury. On the other hand, desorption is a reverse process of adsorption,

468   and conditions unfavorable to adsorption must be favorable conditions for desorption. In our

469   study, lower pH and Cl$^-$ effectively inhibit the adsorption of mercury, so batch regeneration

470   studies were carried out using the mixed solution of 0.1 mol $\cdot$ L^{-1} HCl and 1.0 wt% thiourea as

471 the desorption agent. Adsorption-desorption experiments were performed for ten consecutive

472 cycles to evaluate the regeneration efficiency of PPDCBAs (Fig. 4f). After ten adsorption-

473 desorption cycles, the results show that PPDCBAs still maintain more than 85% of their

474 original adsorption capacity, confirming their adsorption stability.

475 ***3.4. Mechanism of the Hg(II) adsorbed onto PPDCBAs***

476 The experimental results show that PPDCBAs have a much higher adsorption capacity than

477 that of PPDBA, indicating that the introduction of the carboxyl group significantly improved

478 the performance of the adsorbent, which is in agreement with previous studies (Li et al., 2019;

479 Peng et al., 2018). Meanwhile, the extracted adsorption capacities of PPDCBAs are in the

480 following order: PPD4CBA > PPD3CBA > PPD2CBA, which agrees with the ranking of

481 oxygen content in the results of elemental analysis (please see Table 1). Clearly, in the

482 adsorption process, carboxyl groups play a critical role.

483 The PPDCBAs before and after adsorption were analyzed using FT-IR. As shown in Fig. 5,

484 the C=O stretching of PPD2CBA (1755 cm^{-1}) is significantly weakened, and the C=O

485 stretching of PPD3CBA (1698 cm^{-1}) and PPD4CBA (1699 cm^{-1}) are disappeared. At the same

486 time, the C−O stretching of the carboxyl group (1287 cm^{-1} for PPD2CBA, 1266 cm^{-1} for

487 PPD2CBA, 1269 cm^{-1} for PPD4CBA) almost disappear after Hg(II) adsorption. These changes

488 indicate that Hg(II) interacts with carboxyl groups on the surface of PPDCBAs.

489 The XPS spectra were also employed to explore the adsorption mechanism (Fig. 6). In the

490 full-scan spectrum (Fig. 6a-c), the new peaks (Hg 4f) are observed after absorption of Hg(II),

491 and as described in Fig. 6d-f, the binding energy of Hg 4f could be split into two different peaks

492   at 105.59-105.73 eV and 101.55-101.69 eV, which turns out that Hg(II) have been successfully

493   adsorbed by PPDCBAs (Duan et al., 2018; Lin et al., 2019). Fig. 6g shows the high resolution

494   of O 1s peak of PPD2CBA before and after Hg(II) adsorption. The binding energy of C=O

495   (533.60 eV) and C−O (532.36 eV) (Gao et al., 2019) are changed to 532.97 eV and 531.82 eV

496   after adsorbing mercury, respectively, indicating that the oxygen-containing functional groups

497   are complexed with Hg(II). Similar results appear in Fig. 6h and i, which represent the

498   adsorption of Hg(II) onto PPD3CBA and PPD4CBA, respectively. In Fig. 6j, the binding

499   energy of PPD2CBA at 400.84, 400.34 and 398.41 eV, assigning to −N+−, −NH− and −N= (Liu

500   et al., 2019), are shifted to 400.63, 399.65 and 397.98 eV after adsorption, respectively. These

501   changes indicate that nitrogen atoms are also involved in Hg(II) adsorption onto PPD2CBA.

502   Similarly, Fig. 6k and Fig. 6l also share the same conclusion.

503   Moreover, the pH value of the solution after adsorption declined slightly when the initial pH

504   was 2-3. However, the pH value after adsorption increased when the initial pH was 4-7 (Table

505   4). Hence, we speculate that the mercury removal mechanism can be represented by the

506   following complexation between carboxyl groups and Hg(II), as shown in Fig. 7. First, when

507   the pH is low, the main species Hg^{2+} were captured by the carboxyl group (=COOH), and

508   hydrogen ions are released after complexation, which leads to a decrease in the pH of the

509   solution. Then as the pH increases, $Hg(OH)_2$ and $HgOH^+$, which gradually became the

510   dominant species, are trapped by the active site under hydrogen bonding and electrostatic

511   attraction, then Hg^{2+} is chelated with the carboxyl group, and OH⁻ is released at the same time,

512   resulting in an increase in the pH of the solution. Based on the discussion in Section 3.2.6,

513   HgClOH and HgCl$_2$ are the main active species when Cl$^-$ is present, and the adsorption process

514   is depicted in Fig. S10.
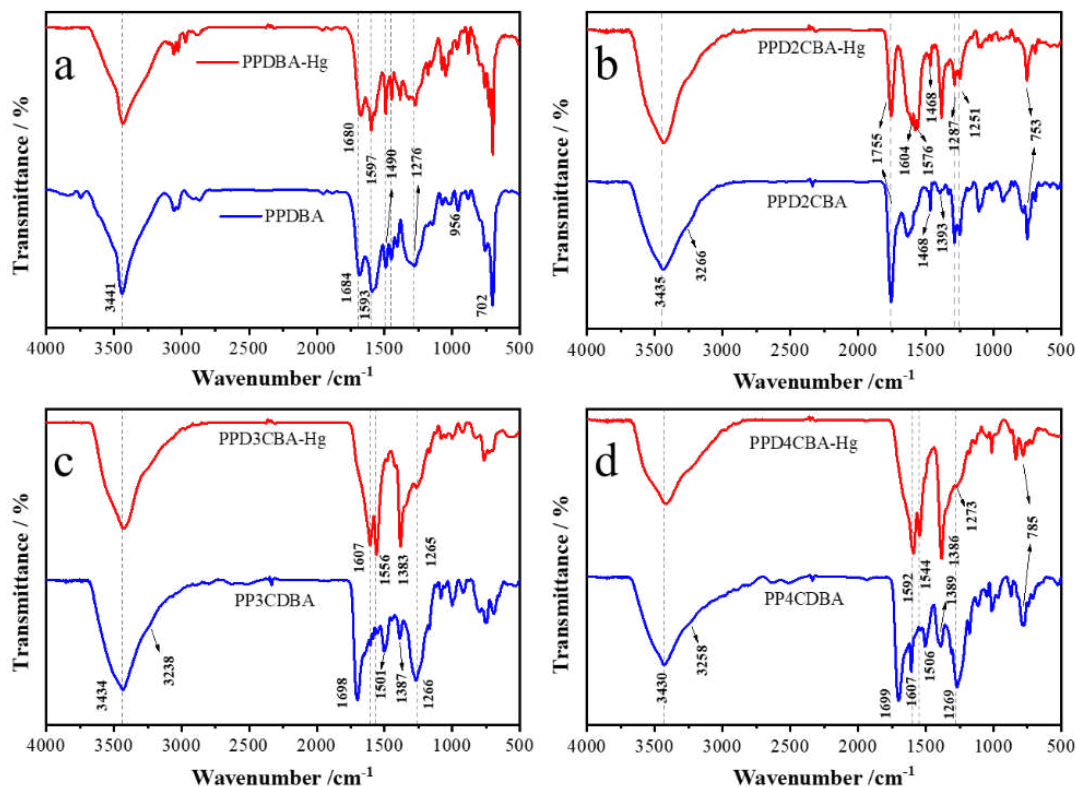
515

516   **Fig. 5.** FT-IR spectra of the samples before and after adsorption: PPDBA (a), PPD2C BA (b),

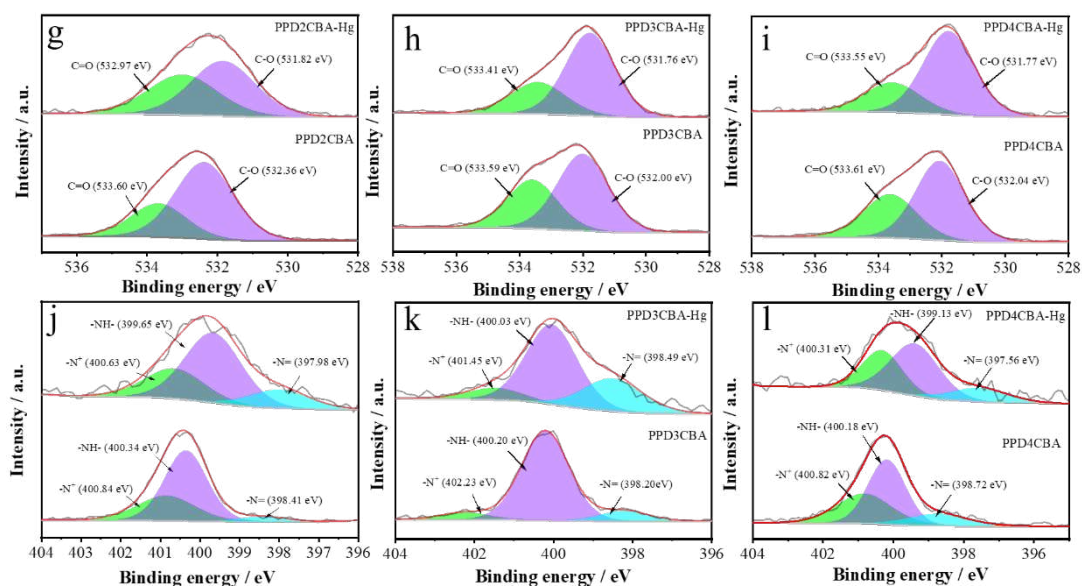517   PPD3CBA (c) and PPD4CBA (d).

518

519
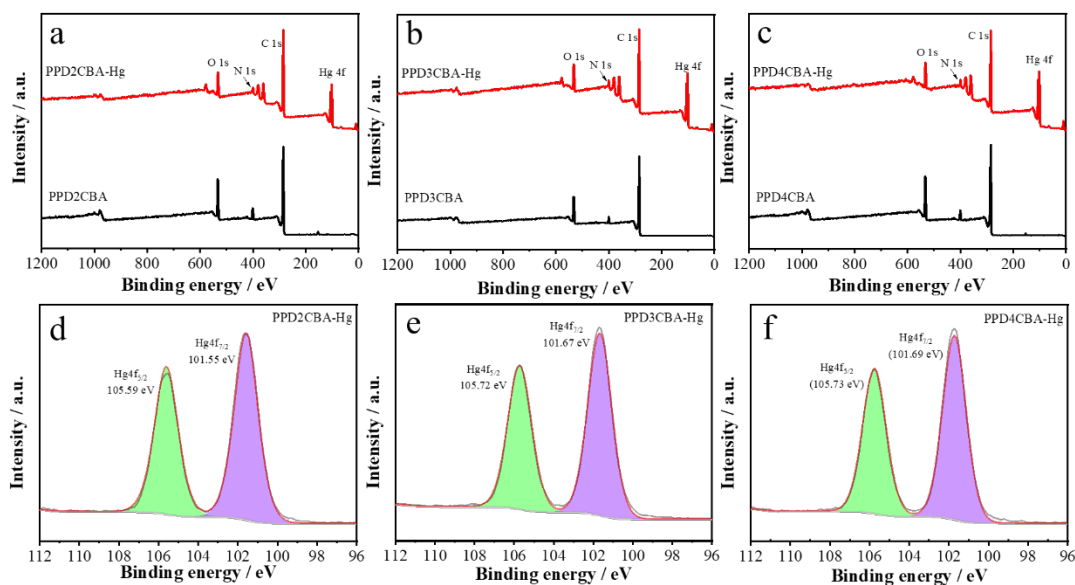
520 **Fig. 6.** Full scan survey XPS spectra: PPD2CBA (a), PPD3CBA (b) and PPD4CBA (c), High

521 resolution spectra of Hg 4f (d-f), O 1s (g-i) and N 1s (j-l) of PPD2CBA, PPD3CBA and

522 PPD4CBA before and after Hg(II) adsorption.

523 **Table 4.** Variation of solution pH before and after mercury adsorption

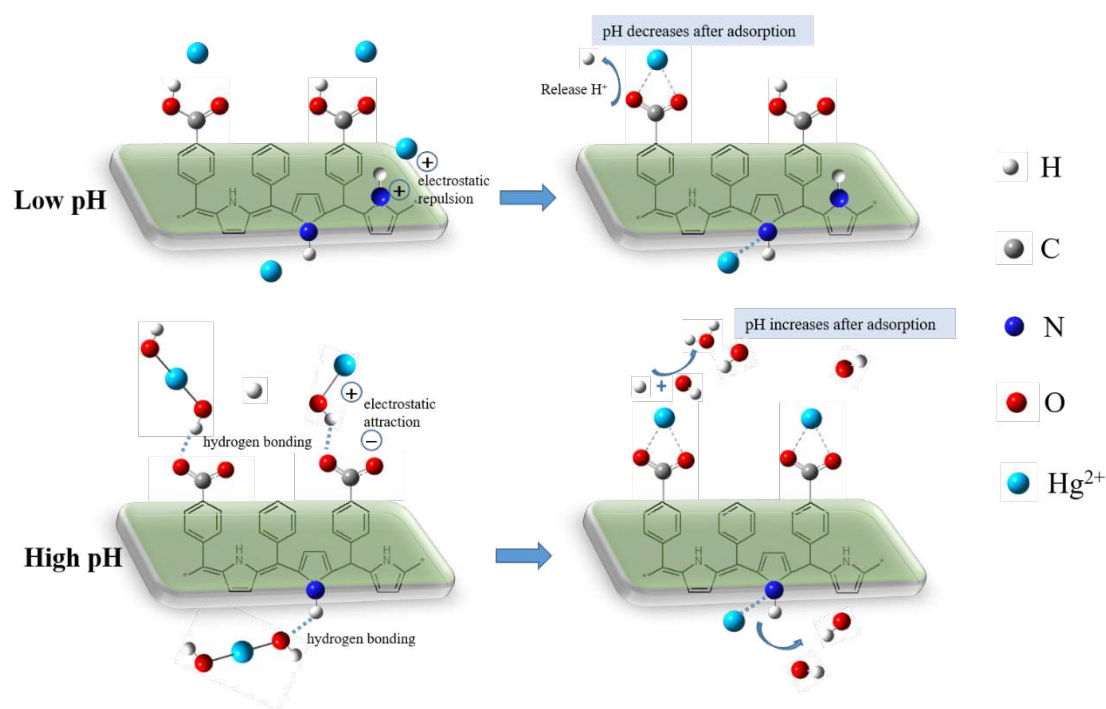| Adsorbents / Initial pH	PPDBA	PPD2CBA	PPD3CBA	PPD4CBA
2	2	2.01	2	2
3	3.02	2.98	2.89	2.88
4	4.28	4.28	4.32	4.19
5	7.38	6.21	6.45	6.09
6	8.15	7.09	6.51	6.30

524

Fig. 7. Possible interactions between carboxyl groups and Hg(II).

DFT calculation was also employed to further confirm the adsorption mechanism. The optimized geometries of the possible complexes formed by poly(pyrrole methane)s with Hg(II) are presented in Fig. 8, and the calculation results are summarized in Table 5. It can be seen that the adsorption energy between the Hg(II) and carboxyl group (from -79.66 to -83.83 kJ·mol^{-1}) is more negative compared with that of the imino group (from -57.29 to -68.54 kJ·mol^{-1}), indicating that the carboxyl groups have a stronger affinity to mercury and play a major role in the mercury capture process, which is consistent with the results of FT-IR analysis. In addition, it can be concluded that the affinity between mercury and the carboxyl group in PPDCBAs confirms the following order: PPD4CBA > PPD3CBA > PPD2CBA, which is consistent with the experimental results of the adsorption capacity. In addition, we further calculated to compare the Mulliken charge distribution of PPDCBAs before and after Hg(II)

537   adsorption (Takjoo et al., 2016; Tellez et al., 2016; Zhang, Z. et al., 2021). Based on the

538   structure-optimized PPDCBAs, Hg^{2+} and complexes of PPDCBAs and Hg^{2+}, static calculations

539   were carried out and obtained the Mulliken charges of mercury in the PPD2CBA-Hg(II),

540   PPD3CBA-Hg(II) and PPD4CBA-Hg(II) to be +1.5254, +1.5149 and +1.5168 e, respectively.

541   Meanwhile, the mulliken charge transfer values of C15, C23, O24 and O25 in PPD2CBA, C15,

542   C23, O24 and O25 in PPD3CBA and C10, C23, O24 and O25 in PPD4CBA are pretty obvious

543   (more positive) after adsorption (Table S7-S9), which indicates that electrons near the active

544   adsorption site (-COO⁻) are transferred and rearranged obviously during the adsorption process,

545   and further verifies the complexation between carboxyl group and Hg(II).

546   Furthermore, Fig. S11 demonstrates the optimized structure of HgClOH complexed with the

547   active site in solution in the presence of Cl⁻ and binding energy and Hg-O bond length in Table

548   S10. The results show that the binding energy of the carboxyl group and HgClOH in

549   PPD2CBA, PPD3CBA and PPD4CBA are -77.47, -81.98 and -83.25 $kJ \cdot mol^{-1}$, which also

550   conforms to the following order: PPD4CBA > PPD3CBA > PPD2CBA, and is consistent with

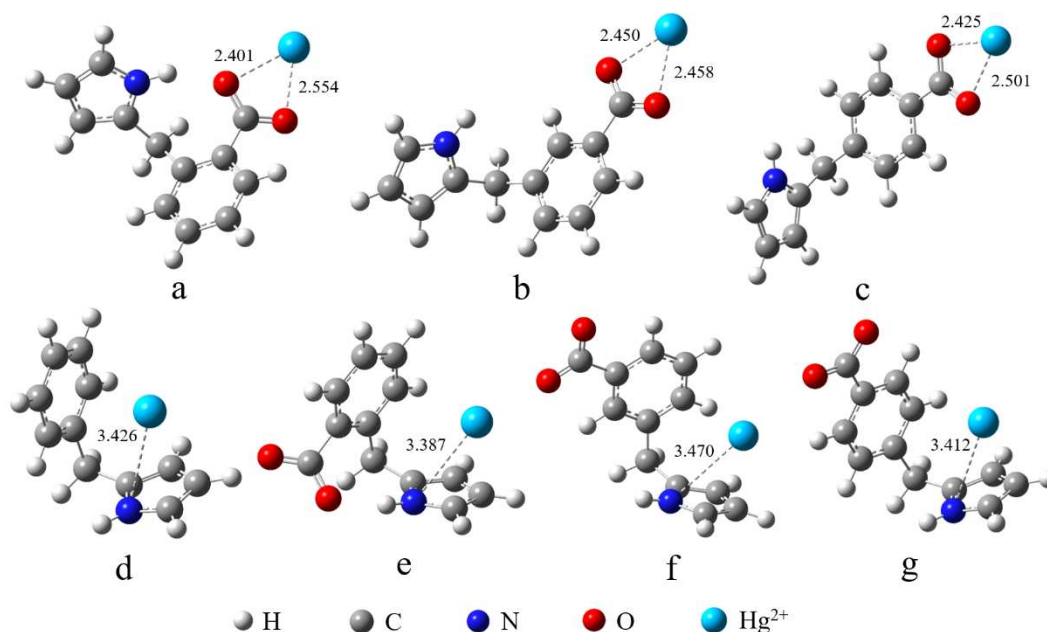551   the experimental results of the adsorption capacity above.

552

Fig. 8. Optimized geometries for the complexes of Hg(II) with carboxyl in PPD2CBA (a), PPD3CBA (b) and PPD4CBA (c), and the complexes of Hg(II) with imino in PPDBA (d), PPD2CBA (e) PPD3CBA (f) and PPD4CBA (g).

Table 5. Binding energy and bond length between mercury and adsorption active sites

Adsorbents	COO-Hg			NH-Hg	
	ΔE_{ad} (kJ·mol^{-1})	Bond length (Å)		ΔE_{ad} (kJ·mol^{-1})	Bond length (Å)
PPDBA	---	---	---	-57.29	3.426
PPD2CBA	-79.66	2.401	2.554	-67.96	3.387
PPD3CBA	-82.67	2.450	2.458	-66.18	3.470
PPD4CBA	-83.83	2.425	2.501	-68.54	3.412

4. Conclusions

In this work, we have demonstrated a strategy to design and tune the highly efficient and selective removal of Hg(II) from aqueous solution by the poly(pyrrole methane)s with phenolic

560   carboxyl groups in the molecular skeleton (PPDCBAs). The saturation adsorption capacity of

561   PPDCBAs with phenolic carboxyl groups for Hg(II) is much greater than that of PPDBA

562   without carboxyl groups, indicating that carboxyl groups are the key to improving the

563   adsorption capacity. Furthermore, the order of adsorption capacity of PPDCBAs was found to

564   be: PPD4CBA > PPD3CBA > PPD2CBA. PPD4CBA has the maximum adsorption capacity

565   for mercury of 1427 mg·g^{-1}, and the fast kinetics for Hg(II) adsorption equilibrium within 100

566   min. Meanwhile, PPDCBAs have good adsorption selectivity for Hg(II) due to introducing a

567   carboxyl group and steric hindrance. Moreover, the stronger affinity of PPDCBAs is ascribed

568   to the complex of heavy metals and the carboxyl groups in the molecular skeleton. DFT

569   calculation further proves that carboxyl and mercury have more negative adsorption energy,

570   suggesting that carboxyl played a key role in mercury capture. It is also shown that PPDCBAs

571   can maintain about 85% of the original adsorption capacity after ten adsorption-desorption

572   cycles, which indicates the recyclability and stability of PPDCBAs for Hg(II) removal. In

573   addition, PPDCBAs could adsorb and remove trace amounts of Hg(II) (10.8 μg·L^{-1}) to meet the

574   drinking water requirement specified by WTO (1 μg·L^{-1}). Our results indicate that PPDCBAs

575   have a strong potential for removing heavy metal ions from aqueous solutions.

576   **CRediT authorship contribution statement**

577   **Zhenyu Wang:** Conceptualization, Investigation, data curation, Writing-original draft

578   preparation.

579   **Yunpeng Liu:** Data curation, Writing - review & editing.

580   **Wenlong Zhang:** Data curation, Writing - review & editing.

581   **Yubing Wang:** Data curation, Writing - review & editing.

582   **Hao Xu:** Writing - review & editing.

583   **Liu Yang:** Writing - review & editing.

584   **Jiangtao Feng:** Supervision, Writing - review & editing, Funding acquisition.

585   **Bo Hou:** Supervision, Writing - review & editing, Funding acquisition.

586   **Mingtao Li:** Software.

587   **Wei Yan:** Writing - review & editing.

588 **Declaration of Competing Interest**

589   The authors declare that they have no known competing financial interests or personal

590 relationships that could have appeared to influence the work reported in this paper.

591 **Acknowledgement**

599   **Appendix A. Supporting information**

600   Supplementary data associated with this article can be found in Supporting Information

601

602

References

Afaneh, A.T., Schreckenbach, G., Wang, F., 2012. Density functional study of substituted (-SH, -S, -OH, -Cl) hydrated ions of Hg^{2+}. Theor. Chem. Acc. 131(4).

Aguila, B., Sun, Q., Perman, J.A., Earl, L.D., Abney, C.W., Elzein, R., Schlaf, R., Ma, S., 2017. Efficient mercury capture using functionalized porous organic polymer. Adv. Mater. 29(31), 1700665.

Ahmad, H., BinSharfan, I., Khan, R.A., Alsalme, A., 2020. 3D Nanoarchitecture of Polyaniline-MoS_2 Hybrid Material for Hg(II) Adsorption Properties. Polym. 12(11), 2731.

Al-Ghouti, M.A., Da'ana, D.A., 2020. Guidelines for the use and interpretation of adsorption isotherm models: A review. J. Hazard. Mater. 393, 122383.

Alguacil, F.J., Escudero, E., 2020. La eliminación de metales tóxicos presentes en efluentes líquidos mediante resinas de cambio iónico. Parte XII: Mercurio(II)/H^+/Lewatit SP112. Rev. Metal. 56(1), 160.

Alguacil, F.J., López, F.A., 2020. Adsorption processing for the removal of toxic Hg(II) from liquid effluents: advances in the 2019 year. Metals 10(3), 412.

Anirudhan, T.S., Divya, L., Ramachandran, M., 2008. Mercury(II) removal from aqueous solutions and wastewaters using a novel cation exchanger derived from coconut coir pith and its recovery. J. Hazard. Mater. 157(2-3), 620-627.

Bachand, S.M., Kraus, T.E.C., Stern, D., Liang, Y.L., Horwath, W.R., Bachand, P.A.M., 2019. Aluminum- and iron-based coagulation for in-situ removal of dissolved organic carbon,

624   disinfection byproducts, mercury and other constituents from agricultural drain water.

625   Ecol. Eng. 134, 26-38.

626   Bakker, J.M., Mac Aleese, L., Von Helden, G., Meijer, G., 2003. The infrared absorption

627   spectrum of the gas phase neutral benzoic acid monomer and dimer. J. Chem. Phys.

628   119(21), 11180-11185.

629   Ballav, N., Das, R., Giri, S., Muliwa, A.M., Pillay, K., Maity, A., 2018. l-cysteine doped

630   polypyrrole (PPy@L-Cyst): A super adsorbent for the rapid removal of Hg^{+2} and efficient

631   catalytic activity of the spent adsorbent for reuse. Chem. Eng. J. 345, 621-630.

632   Bisla, V., Rattan, G., Singhal, S., Kaushik, A., 2020. Green and novel adsorbent from rice straw

633   extracted cellulose for efficient adsorption of Hg (II) ions in an aqueous medium. Int. J.

634   Bio.l Macromol. 161, 194-203.

635   Brown;, J.R., Bancroft;, G.M., Fyfe, W.S., 1979. Mercury removal from water by iron sulfide

636   minerals. An Electron spectroscopy for chemical analysis (ESCA) study. Environ. Sci.

637   Technol. 13, 1142-1144.

638   Caicedo Salcedo, O.D., Vargas, D.P., Giraldo, L., Moreno-Pirajan, J.C., 2021. Study of

639   mercury [Hg(II)] adsorption from aqueous solution on functionalized activated carbon.

640   ACS Omega 6(18), 11849-11856.

641   Chakrabarty, K., Saha, P., Ghoshal, A.K., 2010. Separation of mercury from its aqueous

642   solution through supported liquid membrane using environmentally benign diluent. J.

643   Membr. Sci. 350(1-2), 395-401.

644   Chen, J., Zhu, J., Wang, N., Feng, J., Yan, W., 2019. Hydrophilic polythiophene/SiO$_2$

645   composite for adsorption engineering: Green synthesis in aqueous medium and its

646   synergistic and specific adsorption for heavy metals from wastewater. Chem. Eng. J. 360,

647   1486-1497.

648   Chen, S.Y., Li, Z., Li, K., Yu, X.Q., 2021. Small molecular fluorescent probes for the detection

649   of lead, cadmium and mercury ions. Coord. Chem. Rev. 429, 213691.

650   Choi, H.Y., Bae, J.H., Hasegawa, Y., An, S., Kim, I.S., Lee, H., Kim, M., 2020. Thiol-

651   functionalized cellulose nanofiber membranes for the effective adsorption of heavy metal

652   ions in water. Carbohydr. Polym. 234, 115881.

653   Dai, D., Li, Z., Yang, J., Wang, C., Wu, J., Wang, Y., Zhang, D., Yang, Y., 2019.

654   Supramolecular assembly-induced emission enhancement for efficient mercury(II)

655   detection and removal. J. Am. Chem. Soc. 141(11), 4756-4763.

656   Dong, X., Ma, L.Q., Zhu, Y., Li, Y., Gu, B., 2013. Mechanistic investigation of mercury

657   sorption by Brazilian pepper biochars of different pyrolytic temperatures based on X-ray

658   photoelectron spectroscopy and flow calorimetry. Environ. Sci. Technol. 47(21), 12156-

659   12164.

660   Duan, W., Wang, J., Chang, L., Zhao, L., Tian, Z., Huang, Z., Huang, W., 2018. Adsorption of

661   mercury(II) from water by a novel sPAN fiber containing sulfhydryl, carboxyl and amino

662   groups. RSC Adv. 8(67), 38259-38269.

663   Elovich, S.Y., Larinov, O.G., 1962. Theory of adsorption from solutions of non electrolytes on

664   solid (I) equation adsorption from solutions and the analysis of its simplest form,(II)

665 verification of the equation of adsorption isotherm from solutions. Izv. Akad. Nauk.

666 SSSR, Otd. Khim. Nauk 2(2), 209-216.

667 Freundlich, H., 1907. Über die Adsorption in Lösungen. 57U(1), 385-470.

668 Fu, K., Liu, X., Lv, C., Luo, J., Sun, M., Luo, S., Crittenden, J.C., 2022. Superselective Hg(II)

669 Removal from Water Using a Thiol-Laced MOF-Based Sponge Monolith: Performance

670 and Mechanism. Environ. Sci. Technol. 56(4), 2677-2688.

671 Fu, L., Wang, S., Lin, G., Zhang, L., Liu, Q., Fang, J., Wei, C., Liu, G., 2019. Post-

672 functionalization of UiO-66-NH$_2$ by 2,5-Dimercapto-1,3,4-thiadiazole for the high

673 efficient removal of Hg(II) in water. J. Hazard. Mater. 368, 42-51.

674 Fu, T., Niu, Y., Zhou, Y., Wang, K., Mu, Q., Qu, R., Chen, H., Yuan, B., Yang, H., 2019.

675 Adsorption of Mn(II) from aqueous solution by silica-gel supported polyamidoamine

676 dendrimers: Experimental and DFT study. J. Taiwan Inst. Chem. Eng. 97, 189-199.

677 Fu, Y., Sun, Y., Chen, Z., Ying, S., Wang, J., Hu, J., 2019. Functionalized magnetic

678 mesoporous silica/poly(m-aminothiophenol) nanocomposite for Hg(II) rapid uptake and

679 high catalytic activity of spent Hg(II) adsorbent. Sci. Total Environ. 691, 664-674.

680 Gao, X., Li, M., Zhao, Y., Zhang, Y., 2019. Mechanistic study of selective adsorption of Hg^{2+}

681 ion by porous alginate beads. Chem. Eng. J. 378, 122096.

682 Ge, H., Du, J., 2020. Selective adsorption of Pb(II) and Hg(II) on melamine-grafted chitosan.

683 Int. J. Bio.l Macromol. 162, 1880-1887.

684   Gupta, R., Gupta, S.K., Pathak, D.D., 2019. Selective adsorption of toxic heavy metal ions

685   using guanine-functionalized mesoporous silica [SBA-16-g] from aqueous solution.

686   Microporous Mesoporous Mater. 288, 109577.

687   Hall, K.R., L.C. Eagleton, A. Acrivos, Vermeulen, T., A. Acrivos, Vermeulen, T., 1966. Pore-

688   and solid-diffusion kinetics in fixed-bed adsorption under constant-pattern conditions.

689   Ind. Eng. Chem. Fundam. 5(2), 212-223.

690   Henneberry, Y.K., Kraus, T.E., Fleck, J.A., Krabbenhoft, D.P., Bachand, P.M., Horwath, W.R.,

691   2011. Removal of inorganic mercury and methylmercury from surface waters following

692   coagulation of dissolved organic matter with metal-based salts. Sci. Total Environ. 409(3),

693   631-637.

694   Holmes, P., James, K.A., Levy, L.S., 2009. Is low-level environmental mercury exposure of

695   concern to human health? Sci. Total Environ. 408(2), 171-182.

696   I.D.Reva, S.G.Stepanian, 1995. An infrared study on matrix-isolated benzoic acid. J. Mol.

697   Struct. 349, 337-340.

698   Jainae, K., Sukpirom, N., Fuangswasdi, S., Unob, F., 2015. Adsorption of Hg(II) from aqueous

699   solutions by thiol-functionalized polymer-coated magnetic particles. J. Ind. Eng. Chem.

700   23, 273-278.

701   Ji, Y., Zhang, W., Yang, H., Ma, F., Xu, F., 2021. Green synthesis of poly(pyrrole methane)

702   for enhanced adsorption of anionic and cationic dyes from aqueous solution. J. Colloid

703   Interface Sci. 590, 396-406.

704   Kenawy, I.M., Hafez, M.A.H., Ismail, M.A., Hashem, M.A., 2018. Adsorption of Cu(II),

705   Cd(II), Hg(II), Pb(II) and Zn(II) from aqueous single metal solutions by guanyl-modified

706   cellulose. Int. J. Bio.l Macromol. 107, 1538-1549.

707   Lawrance, G.A., 2013. Introduction to coordination chemistry. John Wiley & Sons.

708   Leus, K., Perez, J.P.H., Folens, K., Meledina, M., Van Tendeloo, G., Du Laing, G., Van Der

709   Voort, P., 2017. UiO-66-$(SH)_2$ as stable, selective and regenerable adsorbent for the

710   removal of mercury from water under environmentally-relevant conditions. Faraday

711   Discuss. 201, 145-161.

712   Li, B., Li, M., Zhang, J., Pan, Y., Huang, Z., Xiao, H., 2019. Adsorption of Hg (II) ions from

713   aqueous solution by diethylenetriaminepentaacetic acid-modified cellulose. Int. J. Bio.l

714   Macromol. 122, 149-156.

715   Li, B., Ye, L., Peng, E., Tan, Z., 2015. Synthesis, conductivity and photophysical properties of

716   soluble low bandgap poly{(3-butyryl)pyrrole-[2,5-diyl(p-hydroxybenzylidene)]}. Synth.

717   Met. 202, 33-38.

718   Li, B., Zhang, Y., Ma, D., Shi, Z., Ma, S., 2014. Mercury nano-trap for effective and efficient

719   removal of mercury(II) from aqueous solution. Nat. Commun. 5, 5537.

720   Lin, C., Luo, W., Luo, T., Zhou, Q., Li, H., Jing, L., 2018. A study on adsorption of Cr (VI) by

721   modified rice straw: Characteristics, performances and mechanism. J. Cleaner Prod. 196,

722   626-634.

723   Lin, G., Hu, T., Wang, S., Xie, T., Zhang, L., Cheng, S., Fu, L., Xiong, C., 2019. Selective

724   removal behavior and mechanism of trace Hg(II) using modified corn husk leaves.

725   Chemosphere 225, 65-72.

726   Liu, Y., Zhang, W., Zhao, C., Wang, H., Chen, J., Yang, L., Feng, J., Yan, W., 2019. Study on

727   the synthesis of poly(pyrrole methane)s with the hydroxyl in different substituent position

728   and their selective adsorption for Pb^{2+}. Chem. Eng. J. 361, 528-537.

729   Lu, X., Huangfu, X., Ma, J., 2014. Removal of trace mercury(II) from aqueous solution by in

730   situ formed Mn-Fe (hydr)oxides. J. Hazard. Mater. 280, 71-78.

731   Luo, F., Chen, J.L., Dang, L.L., Zhou, W.N., Lin, H.L., Li, J.Q., Liu, S.J., Luo, M.B., 2015.

732   High-performance Hg^{2+} removal from ultra-low-concentration aqueous solution using

733   both acylamide-and hydroxyl-functionalized metal-organic framework. J. Mater. Chem.

734   A 3(18), 9616-9620.

735   Lyu, W., Yu, M., Feng, J., Yan, W., 2019. Facile synthesis of coral-like hierarchical polyaniline

736   micro/nanostructures with enhanced supercapacitance and adsorption performance.

737   Polym. 162, 130-138.

738   Marenich, A.V., Cramer, C.J., Truhlar, D.G., 2009. Universal Solvation Model Based on Solute

739   Electron Density and on a Continuum Model of the Solvent Defined by the Bulk Dielectric

740   Constant and Atomic Surface Tensions. The Journal of Physical Chemistry B 113(18),

741   6378–6396.

742   Monahan, F.J., German, J.B., Kinsella, J.E., 1995. Effect of pH and Temperature on Protein

743   Unfolding and Thiol/Disulfide Interchange Reactions during Heat-Induced Gelation of

744   Whey Proteins. J. Agric. Food Chem. 43, 46-52.

745   Mungray, A.A., Murthy, Z.V.P., 2012. Comparative performance study of four nanofiltration

746   membranes in the separation of mercury and chromium. Ionics 18(8), 811-816.

747   Nasimi, S., Baghdadi, M., Dorosti, M., 2020. Surface functionalization of recycled

748   polyacrylonitrile fibers with ethylenediamine for highly effective adsorption of Hg(II)

749   from contaminated waters. J. Environ. Manage. 270, 110883.

750   Nightingale, E.R., 1959. Phenomenological theory of ion solvation. Effective radii of hydrated

751   ions. J. Phys. Chem. 63(9), 1381-1387.

752   Oyetade, O.A., Skelton, A.A., Nyamori, V.O., Jonnalagadda, S.B., Martincigh, B.S., 2017.

753   Experimental and DFT studies on the selective adsorption of Pb^{2+} and Zn^{2+} from aqueous

754   solution by nitrogen-functionalized multiwalled carbon nanotubes. Sep. Purif. Technol.

755   188, 174-187.

756   Peng, Y., Liu, X., Gong, X., Li, X., Liu, Y., Leng, E., Zhang, Y., 2018. Enhanced Hg(II)

757   adsorption by monocarboxylic-acid-modified microalgae residuals in simulated and

758   practical industrial wastewater. Energy Fuels 32(4), 4461-4468.

759   Richard, J.H., Biester, H., 2016. Mercury removal from contaminated groundwater:

760   Performance and limitations of amalgamation through brass shavings. Water Res. 99, 272-

761   280.

762   Saleh, T.A., 2015. Isotherm, kinetic, and thermodynamic studies on Hg(II) adsorption from

763   aqueous solution by silica- multiwall carbon nanotubes. Environ. Sci. Pollut. Res. Int.

764   22(21), 16721-16731.

765   Skyllberg, U., Drott, A., 2010. Competition between disordered iron sulfide and natural organic

766   matter associated thiols for mercury(II)s-an EXAFS study. Environ. Sci. Technol. 44(4),

767   1254-1259.

768   Takjoo, R., Hayatolgheibi, S.S., Amiri Rudbari, H., 2016. Preparation, X-ray structure, spectral

769   analysis, DFT calculation and thermal study on palladium(II) coordination compound

770   with Schiff base derived from S-allyldithiocarbazate. Inorganica Chimica Acta 447, 52-

771   58.

772   Tellez, S.C., Costa, A.C., Jr., Mondragon, M.A., Ferreira, G.B., Versiane, O., Rangel, J.L.,

773   Lima, G.M., Martin, A.A., 2016. Molecular structure, natural bond analysis, vibrational

774   and electronic spectra, surface enhanced Raman scattering and Mulliken atomic charges

775   of the normal modes of [Mn(DDTC)2] complex. Spectrochim Acta A Mol Biomol

776   Spectrosc 169, 95-107.

777   Toru Yahagi, Fujii, A., Ebata, T., Mikami, N., 2001. Infrared spectroscopy of the OH stretching

778   vibrations of jet-cooled salicylic acid and its dimer in S_0 and S_1. J. Phys. Chem. A 105(47),

779   10673-10680.

780   Tran, H.N., You, S.J., Hosseini-Bandegharaei, A., Chao, H.P., 2017. Mistakes and

781   inconsistencies regarding adsorption of contaminants from aqueous solutions: A critical

782   review. Water Resrarch 120, 88-116.

783   Velempini, T., Pillay, K., 2019. Sulphur functionalized materials for Hg(II) adsorption: A

784   review. J. Environ. Chem. Eng. 7(5), 103350.

785   Wang, F., Lu, X., Li, X.Y., 2016. Selective removals of heavy metals (Pb^{2+}, Cu^{2+}, and Cd^{2+})

786   from wastewater by gelation with alginate for effective metal recovery. J. Hazard. Mater.

787   308, 75-83.

788   Wang, J., Guo, X., 2020. Adsorption kinetic models: Physical meanings, applications, and

789   solving methods. J. Hazard. Mater. 390, 122156.

790   Wang, X., Yang, L., Zhang, J., Wang, C., Li, Q., 2014. Preparation and characterization of

791   chitosan-poly(vinylalcohol)/bentonite nanocomposites for adsorption of Hg(II) ions.

792   Chem. Eng. J. 251, 404-412.

793   Worthington, M.J.H., Kucera, R.L., Albuquerque, I.S., Gibson, C.T., Sibley, A., Slattery, A.D.,

794   Campbell, J.A., Alboaiji, S.F.K., Muller, K.A., Young, J., Adamson, N., Gascooke, J.R.,

795   Jampaiah, D., Sabri, Y.M., Bhargava, S.K., Ippolito, S.J., Lewis, D.A., Quinton, J.S.,

796   Ellis, A.V., Johs, A., Bernardes, G.J.L., Chalker, J.M., 2017. Laying waste to mercury:

797   inexpensive sorbents made from sulfur and recycled cooking oils. Chemistry 23(64),

798   16219-16230.

799   Xu, Y., Chen, J., Chen, R., Yu, P., Guo, S., Wang, X., 2019. Adsorption and reduction of

800   chromium(VI) from aqueous solution using polypyrrole/calcium rectorite composite

801   adsorbent. Water Res. 160, 148-157.

802   Yan, X., Li, P., Song, X., Li, J., Ren, B., Gao, S., Cao, R., 2021. Recent progress in the removal

803   of mercury ions from water based MOFs materials. Coord. Chem. Rev. 443, 214034.

804   Zhang, C., Sui, J., Li, J., Tang, Y., Cai, W., 2012. Efficient removal of heavy metal ions by

805   thiol-functionalized superparamagnetic carbon nanotubes. Chem. Eng. J. 210, 45-52.

806   Zhang, J., Zhai, J., Zheng, H., Li, X., Wang, Y., Li, X., Xing, B., 2020. Adsorption, desorption

807   and coadsorption behaviors of sulfamerazine, Pb(II) and benzoic acid on carbon

808   nanotubes and nano-silica. Sci. Total Environ. 738, 139685.

809   Zhang, Y., Bland, G.D., Yan, J., Avellan, A., Xu, J., Wang, Z., Hoelen, T.P., Lopez-Linares,

810   F., Hatakeyama, E.S., Matyjaszewski, K., Tilton, R.D., Lowry, G.V., 2021. Amphiphilic

811   thiol polymer nanogel removes environmentally relevant mercury species from both

812   produced water and hydrocarbons. Environ. Sci. Technol. 55(2), 1231-1241.

813   Zhang, Z., Zhou, Q., Yuan, Z., Zhao, L., Dong, J., 2021. Adsorption of Mg^{2+} and K^+ on the

814   kaolinite (0 0 1) surface in aqueous system: A combined DFT and AIMD study with an

815   experimental verification. Appl. Surf. Sci. 538.

816   Zhao, M., Huang, Z., Wang, S., Zhang, L., Zhou, Y., 2019. Design of l-Cysteine functionalized

817   UiO-66 MOFs for selective adsorption of Hg(II) in aqueous medium. ACS Appl. Mater.

818   Interfaces 11(50), 46973-46983.

819   Zhou, X., Zhou, X., 2014. The Unit Problem in the Thermodynamic Calculation of Adsorption

820   Using the Langmuir Equation. Chem. Eng. Commun. 201(11), 1459-1467.

821   Zhu, H., Shen, Y., Wang, Q., Chen, K., Wang, X., Zhang, G., Yang, J., Guo, Y., Bai, R., 2017.

822   Highly promoted removal of Hg(II) with magnetic $CoFe_2O_4@SiO_2$ core-shell

823   nanoparticles modified by thiol groups. RSC Adv. 7(62), 39204-39215.

824